International Journal of Applied Electromagnetics and Mechanics 15 (2001/2002) 393–402
IOS Press

Smart visualization of multi-scale turbulent structures

Hui Li[a], Yu Zhou[b], Masahiro Takei[c], Yoshifuru Saito[d] and Kiyoshi Horii[e]
[a]*Department of Mechanical Engineering, Kagoshima University, 1-21-40, Korimoto, Kagoshima 890-0065, Japan*
Tel.: +81 99 285 8252; Fax: +81 99 250 3181; E-mail: li@mech.kagoshima-u.ac.jp
[b]*Department of Mechanical Engineering, The Hong Kong Polytechnic University, Hung Hom, Kowloon, Hong Kong, China*
Tel.: +852 2766 6662; Fax: +852 2365 4703; E-mail: mmyzhou@polyu.edu.hk
[c]*Department of Mechanical Engineering, Nihon University, 1-8-14, Kanda Surugadai, Chiyoda-ku, Tokyo 101, Japan*
Tel.: +81 3 3259 0749; Fax: +81 3 3293 8254; E-mail: takei@mech.cst.nihon-u.ac.jp
[d]*Department of Electrical & Electonic Engineering, Hosei University, 3-7-2, Kajino, Koganei, Tokyo 184, Japan*
Tel.: +81 42 387 6200; Fax: +81 42 387 6200; E-mail: ysaitoh@ysaitoh.k.hosei.ac.jp
[e]*Shirayuri Women's College 1-25, Modorigaoka, Chofu-shi, Tokyo 182, Japan*
Tel.: +81 3 3326 7604; Fax: +81 3 3793 7461; E-mail: khorii@shirayuri.ac.jp

Abstract. The vector wavelet multi-resolution technique based on the orthogonal wavelet transform was used to analyze the velocity vector data that were simultaneously obtained by sixteen X-wires in the turbulent near-wake of a circular cylinder at different streamwise positions. The instantaneous velocity vector field is decomposed into the multi-scale structures, and its sectional streamline of various scales is displayed. The large-scale structures in the plane of mean shear are consistent with the well-known Kármán vortices. The structures that correspond to the saddle region between Kármán vortices are identified with the rib-like structures. Even smaller scale structures are also observed. As increasing x/d, the decay of vortical structure and rib-like structure are observed. The topologies of Reynolds stress and RMS vorticity associated with the multi-scale structures are discussed at different downstream positions. It is found that the most significant contribution to Reynolds stress comes from the frequency components of $f \leqslant 219$ Hz at $x/d = 20$. However, the contribution to Reynolds stress coming from the intermediate-scale structure becomes weak at $x/d = 40$. The RMS vorticity components of $f = 875$ Hz is the largest among all components.

1. Introduction

The turbulent near-wake of a circular cylinder has a high degree of organization and is attractive for the purpose of identifying turbulent organized structures and clarifying their contribution to turbulent transfer process. Turbulent structures are characterised by various scales, ranging from so called large-scale vortical structures or vortices, which are dominated by the spanwise vorticity in a turbulent wake, and intermediate-scale structures such as longitudinal or rib-like structures that are primarily aligned in the (x, y)-plane to the smallest Kolmogrov scale structures. Our understanding of the large-scale vortical structures has been improved tremendously in the last three decades or so. This is partly attributed

to the successful development of various identification schemes for deducing these large-scale vortical structures from the turbulent flows, such as the conditional averaging technique [1], the phase-averaging technique [2], the vorticity-based technique [3]; the pattern recognition technique [4], the delocalised conditional sampling and correlation based detection, and the scheme based on critical points [5]. However, it is difficult to use these techniques to deduce intermediate-scale and smaller-scale structures. Flow visualization and hot-wire measurements have highlighted the existence of large-scale organized motions and intermediate-scale structures such as rib structures. However, many aspects of multi-scale structures remain speculative, including the dynamical role and the spatial relationship between ribs and spanwise structure.

In the past decade, there has been a growing interest in using wavelet technique for the analysis of turbulent flow data [6]. This technique allows time-space and frequency-space analyses to be combined and produces a potentially clearer picture of time-frequency localization of turbulent structures. However, few investigations concerned the extraction of turbulent structures in terms of time and scale from the measured velocity vector field. To solve this problem, Li and Zhou [7] developed the vector wavelet multi-resolution analysis to the analysis of turbulent flow velocity data. This technique is unique in that turbulent structures of different scales can be separated and characterised, and is reliable and effective for analysis of multi-scale turbulent structures in time and frequency spaces. The aim of the present work is to apply this technique to analyze the experimental data of the near-wake of a circular cylinder further, for identifying the turbulent structures of various scales and providing both qualitative and quantitative information on the multi-scale turbulent structures at different downstream positions.

2. Vector wavelet multi-resolution analysis

Let us consider a two-dimensional vector field $\vec{f}(x_1, x_2)$ and a two-dimensional orthogonal wavelet basis

$$\Psi_{m_1,n_1;m_2,n_2}(x_1, x_2) = 2^{-(m_1+m_2)/2}\Psi(2^{-m_1}x_1 - n_1)\Psi(2^{-m_2}x_2 - n_2), \tag{1}$$

where $\Psi(x)$ is an one-dimensional orthogonal wavelet basis. There are functions, for example, Meyer, Daubechies, Coifman, Battle-Lemarie, Baylkin and spline functions, may be used as the orthogonal wavelet basis.

The two-dimensional discrete vector wavelet transform is defined as

$$\overrightarrow{Wf}_{m_1,n_1;m_2,n_2} = \sum_i \sum_j \vec{f}(x_1^i, x_2^j)\Psi_{m_1,n_1;m_2,n_2}(x_1^i, x_2^j) \tag{2}$$

The reconstruction of the original vector field can be achieved by using

$$\vec{f}(x_1, x_2) = \sum_{m_1}\sum_{m_2}\sum_{n_1}\sum_{n_2} \overrightarrow{Wf}_{m_1,n_1;m_2,n_2}\Psi_{m_1,n_1;m_2,n_2}(x_1, x_2). \tag{3}$$

The procedure of the vector wavelet multi-resolution analysis can be summarised in two steps:

(1) Wavelet coefficients of vector data are computed based on the discrete vector wavelet transform of Eq. (2).
(2) Inverse vector wavelet transform of Eq. (3) is applied to wavelet coefficients at each wavelet level, and vector components are obtained at each wavelet level or scale.

In this paper, we use the Daubechies family with index $N = 20$, which is not only orthogonal, but also has smoothness and compact support, as orthogonal wavelet basis.

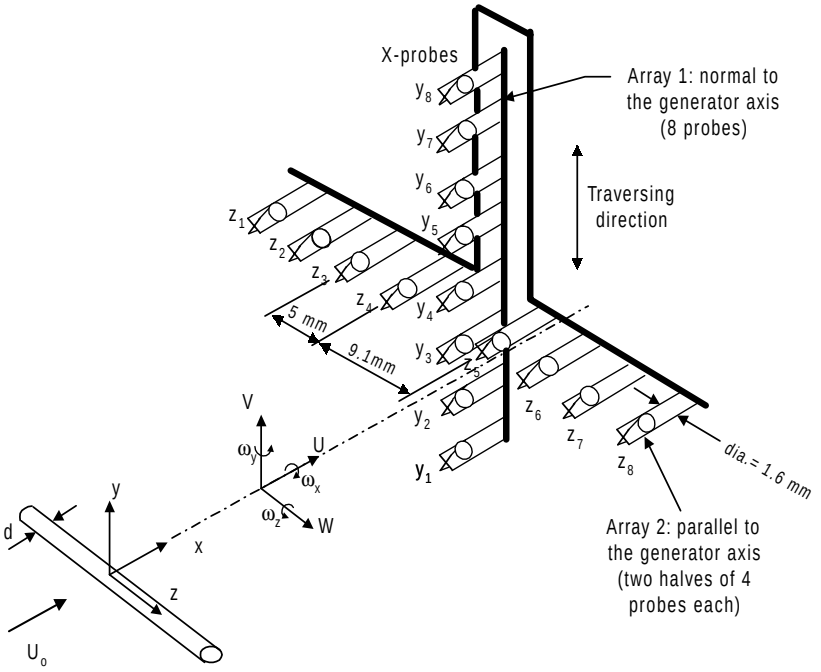

Fig. 1. Experimental arrangement.

3. Experimental setup

Experiments were carried out in a low turbulence wind tunnel with a 2.4 m long working section ($0.35\ \mathrm{m} \times 0.35\ \mathrm{m}$). A circular cylinder ($d = 12.5$ mm) was installed in the mid-plane and spanned the full width of the working section. The experimental arrangement is shown in Fig. 1. Two orthogonal arrays, each of eight X-wires, were used. Eight X-wires were aligned in the (x, y)-plane, i.e., the plane of mean shear, and eight in the (x, z)-plane, which is parallel to both the cylinder axis and the streamwise direction. The sixteen X-wires allow velocity fluctuations u and v in the (x, y)-plane and u and w in the (x, z)-plane to be obtained simultaneously with a sampling frequency of $f_s = 3.5$ kHz. The nominal spacing between X-wires was about 5 mm. Measurements were made at $x/d = 20$ and 40 (x is the streamwise distance downstream of the cylinder) with a constant free stream velocity ($U_0 = 6.7$ m/s). The corresponding Reynolds number Re was 5600. More details of the experiments have been given in Zhou et al. [8].

4. Instantaneous multi-scale structures

In order to gain insight into the multi-scale turbulent structures, we apply vector wavelet multi-resolution analysis to the measured velocity vector data of a turbulent wake. The instantaneous velocity vector $\vec{u}(x, y, z, t)$ is decomposed into thirteen compositions $\vec{u}_i(x, y, z, t)$ within different scale ranges based on the vector wavelet multi-resolution analysis. Therefore, the instantaneous velocity vector $\vec{u}(x, y, z, t)$ can be written as the sum of the time averaging velocity vector $\vec{U}(x, y, z)$ and velocity vector

compositions $\vec{u}_i(x, y, t)$ i.e.,

$$\vec{u}(x, y, z, t) = \vec{U}(x, y, z) + \sum_{i=1}^{13} \vec{u}_i(x, y, z, t) \tag{4}$$

Within these scale ranges the spanwise component of vorticity at each of the scales can be also defined in terms of the derivatives of the instantaneous velocity components $u = U + u_i$ and $v \cong v_i$ ($V \cong 0$), where an overbar denotes time averaging and the index, i, stands for scale, viz.

$$\omega_{zi} = \frac{\partial v_i}{\partial x} - \frac{\partial(U + u_i)}{\partial y} \approx \frac{\Delta v_i}{\Delta x} - \frac{\Delta(U + u_i)}{\Delta y}, \tag{5}$$

In above equation, $\Delta y \approx 5.0$ mm is spacing between two X-wires; $\Delta x = -U_c \Delta t$, where $\Delta t = 1/f_s$ and $U_c = 0.87U_0$ [9] is the average convection velocity.

Figure 2(a)–(d) shows the decomposed sectional streamlines that were calculated from the components of velocity vector for wavelet levels 9 to 12 in the (x, y)-plane at $x/d = 20$. The central frequencies of these five levels are 109, 219, 438 and 875 Hz, respectively, representing turbulence structures of different scales. Figure 2(e) displays the corresponding measured streamlines, i.e., original data before decomposition. The flow direction is right to left. Figure 2(a) exhibits six vortical structures at $tU_c/d \approx 2, 6, 10.5, 15, 19$ and 23.5. These structures correspond quite well to the large-scale structures in Fig. 2(e), which occur at frequencies around the average frequency (109 Hz) of Kármán vorticies. They are apparently the uppermost and energy-containing structures. The agreement between the measured velocity and the decomposed data of the 109 Hz range provides a validation for the present data analysis technique. The streamlines in Fig. 2(b) show a number of structures that are smaller than those in Fig. 2(a). Some of them are the small vortices that are contained in Kármán vortices, e.g., at $tU_c/d \approx 6, 11, 15.5, 19.5$ and 22.5. Others correspond to the saddle regions, e.g., at $tU_c/d \approx 3.5, 8, 12, 17$ and 21, between the vortices. These are consistent with the occurrence of rib structures, because the rib structure is located between successive spanwise structures. As the central frequency is increased from 438 to 875 Hz (Fig. 2(b)–(d)), a number of even smaller scale structures are identifiable. These structures appear to cover the whole field. However, their occurrence is rather periodical. Note that it is difficult to identify the structures smaller than Kármán vortices in the original streamlines (Fig. 2(e)).

At the downstream location of $x/d = 40$, the sectional streamlines for the central frequencies of 109, 219, 438 and 875 Hz in the (x, y)-plane are shown in Fig. 3. The measured streamlines are also plotted in Fig. 3(e). The irregular structures with various scales can be seen in Fig. 3(e). However, in Fig. 3(a) we can easily identify five vortical structures that occur around the average frequency (109 Hz) of Kármán vorticies at $tU_c/d \approx 1, 7, 13, 17.5$ and 21. The considerable dispersions in size and strength happen in these vortical structures, and the locations of these vortical structures are closed to the mid-plane. At the central frequencies of 219 Hz in Fig. 3(b), four small vortices appear at $tU_c/d \approx 2.5, 7, 12$ and 20.5. Two saddle regions can be clearly observed at $tU_c/d \approx 14.5$ and 24. This indicates the occurrence of rib structures at $x/d = 40$. At the higher central frequency ranged from 438 to 875 Hz in Fig. 3(b)–(d), a number of even smaller scale structures are identified in the whole field.

5. Multi-scale reynolds stresses

The time-averaged shear stress components at different central frequency at $x/d = 20$, which are normalized by U_0^2, are shown in Fig. 4(a). The distribution of $\overline{uv}$ component at each frequency is

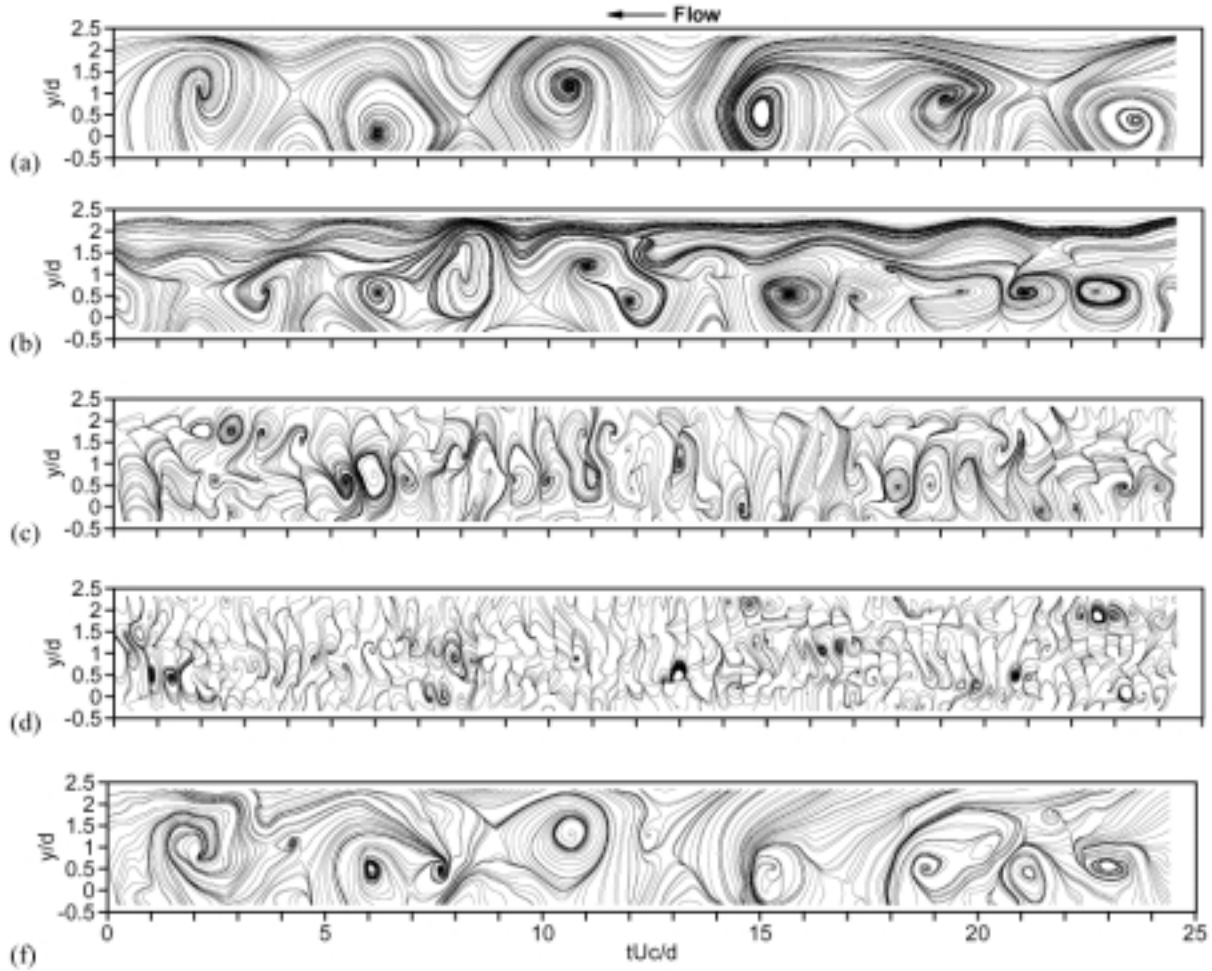

Fig. 2. Instantaneous streamlines in the (x, y)-plane at $x/d = 20$: (a) $f = 109$ Hz; (b) $f = 219$ Hz; (c) $f = 438$ Hz; (d) $f = 875$ Hz; (f) Measured data.

similar to that of the measured data. The $\overline{uv}$ component decreases when increasing frequency, and varies greatly with the central frequency. In the range of high frequency ($f > 438$ Hz), $\overline{uv}$ component decreases rapidly with increasing the frequency. The $\overline{uv}$ component of 109 Hz remains everywhere largest in all components. The $\overline{uv}$ component of 219 Hz is also evidently larger than other components of $f \geqslant 438$ Hz. This indicates that the contribution to the total shear stresses is greater from the large- and intermediate-scale structures. The peaks of $\overline{uv}$ components at 109 and 219 Hz appear around $y/d = 1.0$, which correspond to the averaged position of the vortex and saddle-point or rib-like structure. At the downstream of $x/d = 40$, as shown in Fig. 4(b), $\overline{uv}$ component of 109 Hz still remains the largest among all components. This component makes the greatest contribution to the total shear stress. The $\overline{uv}$ component of 219 Hz, which represents the intermediate-scale structure, becomes weak and less contribution to the total Reynolds stress. This may imply the decay of vortical structure and rib-like structure within this scale range as x/d increases.

The distributions of time-averaged normal stress components $\overline{u^2}$ at various frequency for $x/d = 20$

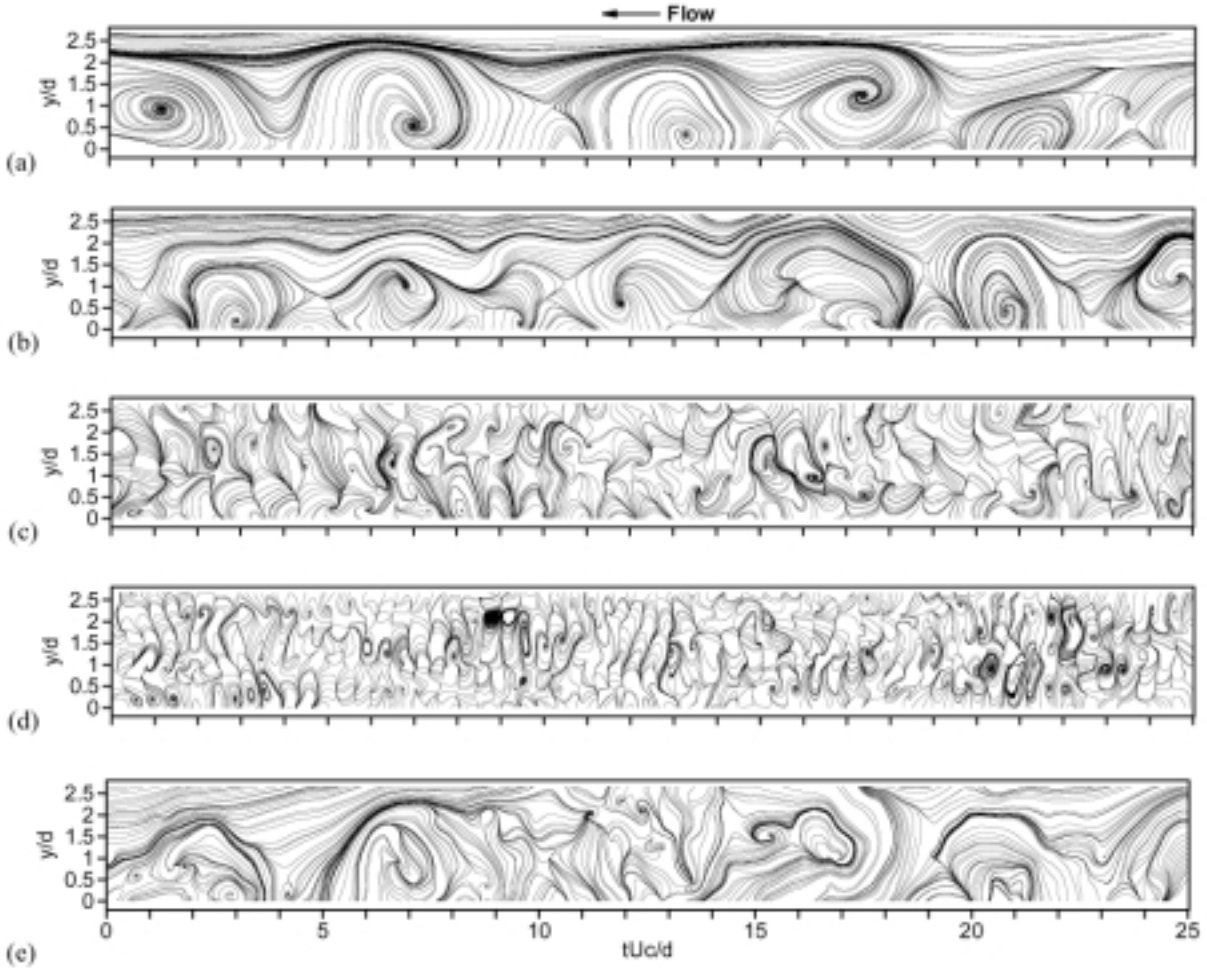

Fig. 3. Instantaneous streamlines in the (x, y)-plane at $x/d = 40$: (a) $f = 109$ Hz; (b) $f = 219$ Hz; (c) $f = 438$ Hz; (d) $f = 875$ Hz; (f) Measured data.

and 40 are plotted in Fig. 5. At the location of $x/d = 20$, as shown in Fig. 5(a), the distribution of $\overline{u^2}$ component at each frequency is similar to that of the total normal stress for $f \leqslant 438$ Hz. However, $\overline{u^2}$ components decrease with y for $f > 438$ Hz. As the central frequency increases, $\overline{u^2}$ component decreases, but $\overline{u^2}$ component of 219 Hz is higher than that of 109 Hz in the range of $y/d < 1.0$. This implies that the contribution to $\overline{u^2}$ from the intermediate-scale structures is greater than that from large-scale structures due to the occurrence of the rib-like structures. At the downstream of $x/d = 40$, only the large-scale component of $\overline{u^2}$ around the average frequency (109 Hz) of Kármán vorticies is similar to that of the total normal stress. The $\overline{u^2}$ component of intermediate-scale structure around the central frequency of 219 Hz is smaller than that of large-scale structure, and its profile is similar to other components of $f \geqslant 438$ zH. This indicates that the greatest contribution to the total normal stress comes from the component of large-scale structure at this location.

Figure 6 shows the distribution of $\overline{v^2}$ component at each frequency at locations of $x/d = 20$ and 40. The profiles of $\overline{v^2}$ component are also similar to that of the total crossflow normal stress, and vary greatly

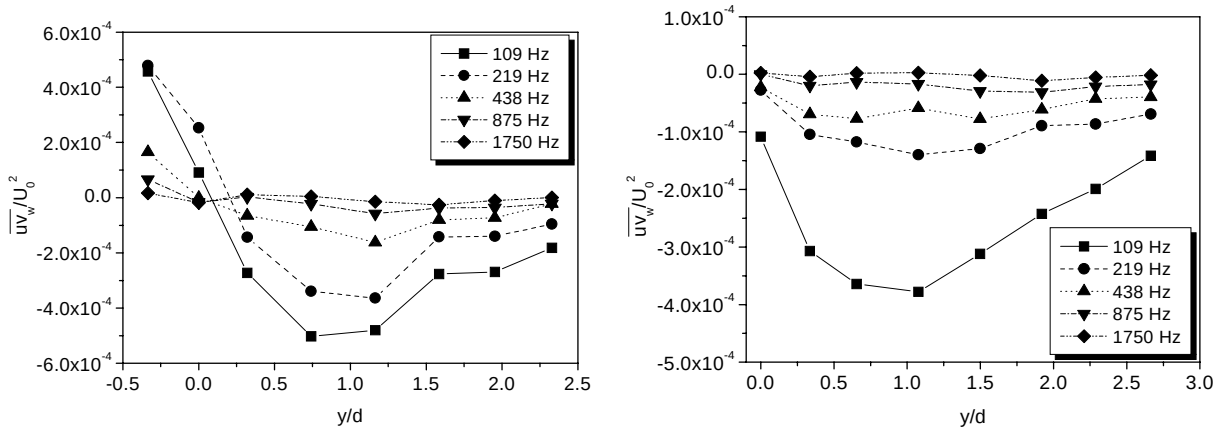

(a) *x/d*=20 (b) *x/d*=40

Fig. 4. Time-averaged shear stress components at different central frequency.

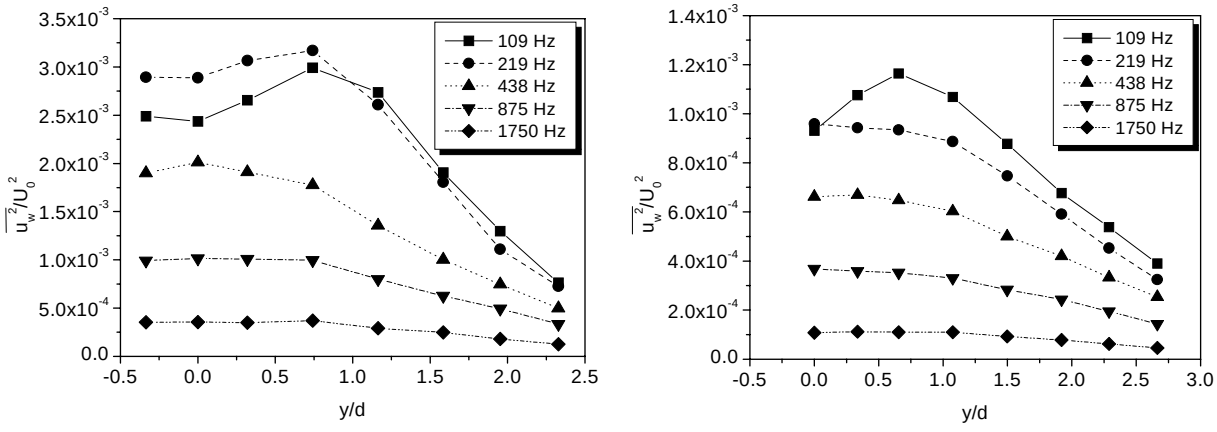

(a) *x/d*=20 (b) *x/d*=40

Fig. 5. Time-averaged normal stress components at different central frequency.

with y. At the location of $x/d = 20$, as shown in Fig. 6(a), the largest $\overline{v^2}$ component for the central frequency of 219 Hz can be observed in the range of $y/d < 1.5$, although $\overline{v^2}$ component decreases with increasing the central frequency. This implies that the most significant contribution to the total crossflow normal stress appears to come from the rib-like structure. When $f \geqslant 438$ Hz, $\overline{v^2}$ component decreases rapidly with frequency and the contribution to $\overline{v^2}$ becomes weak. At the location of $x/d = 40$, $\overline{v^2}$ component around the central frequency of 109 Hz becomes largest among the various frequency components, and makes the greatest contribution to the total crossflow normal stress.

From above results presented here, it can say that the most significant contribution to Reynolds stress appears to come from frequency components of $f \leqslant 219$ Hz, i.e., large-scale and rib-like structures, at the downstream of $x/d = 20$. Therefore, the most significant contribution to turbulent energy does not only come from the large-scale motions, but also comes from intermediate-scale motion. However, as increasing x/d, the contribution to Reynolds stress coming from the intermediate-scale structure becomes weak because the strength of rib decays rapidly.

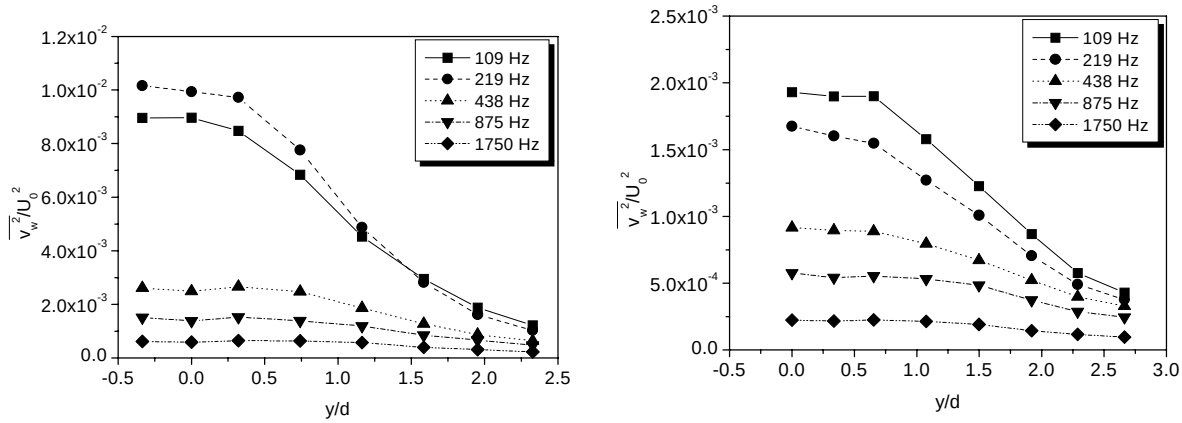

(a) *x/d*=20 (b) *x/d*=40

Fig. 6. Time-averaged crossflow normal stress components at different central frequency.

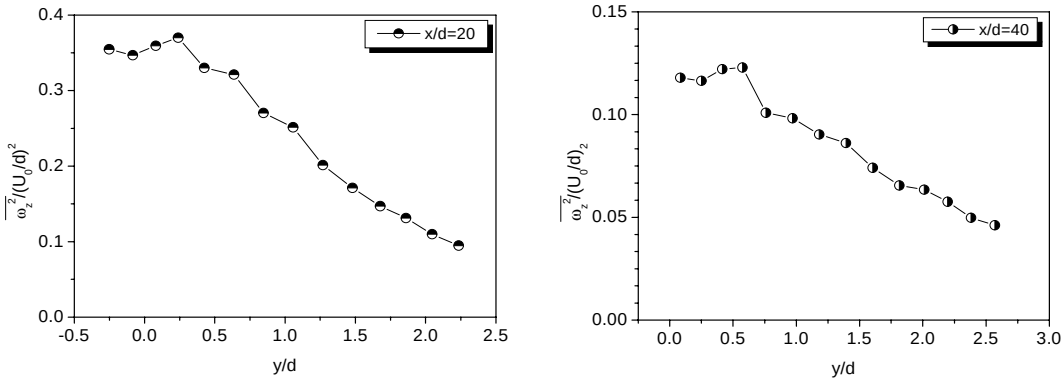

(a) *x/d*=20 (b) *x/d*=40

Fig. 7. Total RMS value of vorticity.

6. Multi-scale vorticity

Figure 7 shows the distribution of the total RMS value of vorticity that are normalized by the factor $(U_0/d)^2.\overline{\omega_z^2}$ first increase away from the centerline up to a maximum near $y/d = 0.25$ and 0.5 at locations of $x/d = 20$ and 40, respectively, before decreasing towards the edge of the wake. The total RMS value of vorticity decreases along the downstream direction. In order to examine the dynamical role of various frequency components of vorticity, the distribution of RMS vorticity components $\overline{\omega_{zw}^2}$ at locations of $x/d = 20$ and 40 are plotted as a function of the central frequency in Fig. 8. It is found that at the location of $x/d = 40$ the variances of RMS vorticity components with y/d are qualitatively similar to the total RMS value of vorticity. The variances of RMS vorticity components within range of $f \leqslant 219$ Hz at the location of $x/d = 20$, however, decrease monotonically towards the edge of the wake, which are different from the total RMS value of vorticity. The smallest value for the RMS vorticity component of $f = 109$ Hz indicates that the large-scale motion exhibits less contribution to the RMS vorticity than other components for both of two locations. However, the RMS vorticity component of $f = 219$ Hz is slightly larger than that of $f = 1750$ Hz and is close to that of $f = 438$ Hz in the centerline region at

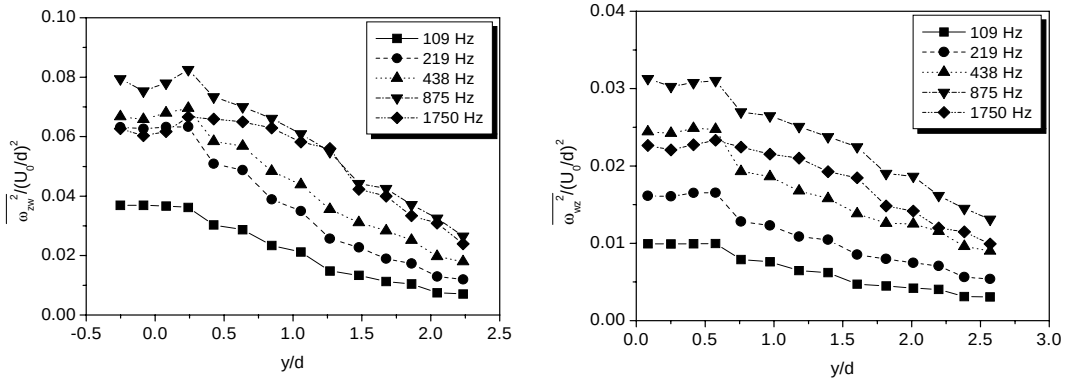

(a) *x/d*=20 (b) *x/d*=40

Fig. 8. RMS vorticity components at different central frequency.

$x/d = 20$. This is due to the contribution from the rib-like structures in the intermediate-scale motion. When increasing the central frequency, the $\overline{\omega_{zw}^2}$ first increases up to a maximum at $f = 875$ Hz, and then decreases. The magnitude of $\overline{\omega_{zw}^2}$ at $f = 875$ Hz exhibits the largest everywhere for both of two locations. The peak of $\overline{\omega_z^2}$ appeared in the total RMS value of vorticity in Fig. 7 results from the vorticity components of $f \geqslant 438$ Hz, i.e., the small-scale structure.

7. Conclusions

(1) The large-scale structures are consistent with the well-known Kármán vortices. The structures that correspond to the saddle region between successive Kármán vortices are identified with the rib-like structures. Even smaller scale structures are also observed.
(2) As increasing x/d, the decay of vortical structure and rib-like structure are observed from the instantaneous multi-scale sectional streamlines.
(3) The most significant contribution to Reynolds stress comes from frequency components of $f \leqslant 219$ Hz, i.e., large-scale and rib-like structures, at the downstream of $x/d = 20$. However, the contribution to Reynolds stress coming from the intermediate-scale structure becomes weak at the downstream of $x/d = 40$.
(4) The RMS vorticity components decrease along downstream direction. The component of $f = 875$ Hz is the largest among all components.
(5) The RMS vorticity component of $f = 109$ Hz exhibits less contribution to the total RMS vorticity than other components.
(6) The contribution to the total RMS vorticity coming from the component of $f = 219$ Hz becomes weak in the centerline region as increasing x/d.

References

[1] B. Cantwell and D. Coles, An Experimental Study of Entrainment and Transport in the Turbulent Near Wake of a Circular Cylinder, *J. Fluid Mech.* **136** (1983), 321–374.
[2] M. Kiya and M. Matsumara, Incoherent Turbulence Structure in the Near Wake of a Normal Plate, *J. Fluid Mech.* **190** (1988), 343–356.

[3] A.K.M.F. Hussain and M. Hayakawa, Education of Large-Scale Organised Structures in a Turbulent Plane Wake, *J. Fluid Mech.* **80** (1987), 193–229.
[4] Y. Zhou and R.A. Antonia, A Study of Turbulent Vortices in the Wake of a Cylinder, *J. Fluid Mech.* **253** (1993), 643–661.
[5] Y. Zhou and R.A. Antonia, Critical Points in a Turbulent Near-Wake, *J. Fluid Mech.* **275** (1994), 59–81.
[6] H. Li, Identification of Coherent Structure in Turbulent Shear Flow with Wavelet Correlation Analysis, *ASME Journal of Fluids Engineering* **120** (1998), 778–785.
[7] H. Li. and Y. Zhou, *Multi-Scale Structures in a Turbulent Near-Wake*, Advances in Turbulence VIII, CIMNE Press, 2000, pp. 245–248.
[8] Y. Zhou, W.K. Tsang and R.A. Antonia, Vortical Structures in a Turbulent Far-Wake: Effect of Reynolds Number, *Fluid Dynamics Research* **25** (1999), 293–314.
[9] Y. Zhou and R.A. Antonia, Convection Velocity Measurements in a Cylinder Wake, *Experiments in Fluids* **13** (1992), 63–70.